CSEM inversion using the correspondence principle: the adjoint-state approach

Adriany Tiffany Moura Reis Valente* (UFPA, Faculdade de Geofísica, Belém (PA)), Deivid Nascimento (Petrobrás), Jessé Carvalho Costa (UFPA, Faculdade de Geofísica, Belém (PA), Brasil & INCT-GP)

Abstract

The correspondence principle permits the modeling of marine controlled-source electromagnetic (CSEM) data solving Maxwell's equations numerically using time-domain finite-difference in a dielectric media. Attractive features of this method include: I) modeling multi-frequency data in a single finite-difference simulation, II) low-memory demand when compared to solving Maxwell's equation in a conductive media in 3D, there is no need to solve a large linear system for each frequency; III) it can be implemented very efficiently in distributed nodes with GPU accelerators. We investigate the application of the correspondence principle to the inversion of CSEM data. We start revising the adjoint state method to establish the relation between the adjoint fields in the conductive medium and the fictitious dielectric medium derived from the correspondence principle. Then, we derive the expression for the gradient of least-squares objective function from the adjoint-state solution in the fictitious domain. This derivation, although straightforward shows that the computation of adjoint-fields in the fictitious dielectric medium presents subtle differences relative to the forward modeling of EM fields using the correspondence principle. We validate this approach through the inversion of a CSEM synthetic data set, computed for a simple reservoir model in 3D. Our numerical experiments also evaluate the effects of regularization, using model reparameterization, on the convergence and stability of the iterations of the optimization algorithm.

Introduction

The electromagnetic methods are widely investigated to aid in hydrocarbon exploration. Mainly for the exploration of frontier regions, where the structural complexity and heterogeneous overburden might present significant challenges to seismic imaging and inversion (Meju et al., 2018). This interest sustains the research for the development of effective and efficient algorithms for the inversion of CSEM data (Hansen et al., 2016; Meju et al., 2018, 2019; Cai et al., 2021; Hoversten et al., 2021).

The algorithms for CSEM inversion in the recent literature differ mostly in the algorithm to solve the modeling of EM data and on the regularization strategy to stabilize the linearized iterations (Hansen et al., 2016; Meju et al., 2019; Hoversten et al., 2021; Cai et al., 2021). We investigated the inversion of CSEM data based on the modeling algorithm proposed by Mittet (2010). Accordingly, we present a derivation for the gradient of the objective-function fully based on the principle of correspondence (de Hoop, 1996). This derivation, based on the adjoint-state method (Plessix, 2006; Chavent, 2010), shows how we can use the same forward algorithm proposed by Mittet (2010) to compute the gradient with just a reverse-time modeling. Our algorithm also differs on how to regularize the inversion iterations. We use the model reparameterization proposed by Harlan (1995); Claerbout (2003) to stabilize the non-linear inversion, an import feature of the method is to dispense the need to select, usually by trial and error, a regularization parameter to enforce some model penalization without degrade the data-fitting (Lima et al., 2019).

We also evaluate two optimization algorithm. The traditional LBFGS(Zhu et al., 1997; Nguyen et al., 2016) and the much less memory demanding ADAM algorithm (Kingma and Ba, 2014). Our numerical experiments show that both algorithm were successful in fitting the observations and correctly localizing the inversion target. Moreover, model reparameterization was very effective in enforcing the stabilization and helping to accelerate the convergence of the inversion iterations.

Methodology

Forward modeling using the Correspondence Principle

The Maxwell's equations in the time domain for a conductive medium in the quasi-static limit are:

$$-\nabla\times\mathbf{H}(\mathbf{x},t)+\boldsymbol{\sigma}(\mathbf{x})\mathbf{E}(\mathbf{x},t) = -\mathbf{J}(\mathbf{x},t), \quad (1)$$

$$\nabla\times\mathbf{E}(\mathbf{x},t)+\mu\partial_t\mathbf{H}(\mathbf{x},t) = -\mathbf{K}(\mathbf{x},t), \quad (2)$$

where $\mathbf{E}(\mathbf{x},t)$ and $\mathbf{H}(\mathbf{x},t)$ represent the electric and magnetic fields, respectively, $\boldsymbol{\sigma}(\mathbf{x})$ is conductivity tensor and μ the magnetic permeability; the injection source distributions, $\mathbf{J}(\mathbf{x},t)$ and $\mathbf{K}(\mathbf{x},t)$, represent the electric and magnetic current density, respectively. We use this convention for Fourier transform:

$$F(\omega) = \int_{-\infty}^{+\infty} dt\, f(t)e^{i\omega t}, \quad (3)$$

$$f(t) = \frac{1}{2\pi}\int_{-\infty}^{+\infty} d\omega F(\omega)e^{-i\omega t}, \quad (4)$$

when mapping back and forth from time to frequency. The Maxwell equations in the frequency domain are,

$$-\nabla\times\mathbf{H}(\mathbf{x},\omega)+\boldsymbol{\sigma}(\mathbf{x})\mathbf{E}(\mathbf{x},\omega) = -\mathbf{J}(\mathbf{x},\omega), \quad (5)$$

$$\nabla\times\mathbf{E}(\mathbf{x},\omega)-i\omega\mu\mathbf{H}(\mathbf{x},\omega) = -\mathbf{K}(x,\omega). \quad (6)$$

The correspondence principle (de Hoop, 1996) establishes the relationship between equations (5) and (6) with the Maxwell equations in frequency-domain for a non-conductive dielectric medium:

$$-\nabla\times\mathbf{H}'(\mathbf{x},\omega')-i\omega\varepsilon'(\mathbf{x})\mathbf{E}'(\mathbf{x},\omega')=-\mathbf{J}'(\mathbf{x},\omega), \quad (7)$$

$$\nabla\times\mathbf{E}'(\mathbf{x},\omega')-i\omega'\mu\mathbf{H}'(\mathbf{x},\omega')=-\mathbf{K}'(\mathbf{x},\omega'). \quad (8)$$

Following de Hoop (1996), the mapping from the real conductive medium, equations (5) and (6), to its corresponding fictitious dielectric model, equations (7) and (8), can be achieved defining:

$$\omega'\equiv(1+i)\sqrt{\omega\omega_0}, \quad (9)$$

$$\varepsilon'(\mathbf{x})\equiv\boldsymbol{\sigma}(\mathbf{x})/(2\omega_0) \quad (10)$$

$$\mathbf{E}'(\mathbf{x},\omega')\equiv\mathbf{E}(\mathbf{x},\omega), \quad (11)$$

$$\mathbf{H}'(\mathbf{x},\omega')\equiv\sqrt{\frac{-i\omega}{2\omega_0}}\mathbf{H}(\mathbf{x},\omega), \quad (12)$$

$$\mathbf{J}'(\mathbf{x},\omega')\equiv\sqrt{\frac{-i\omega}{2\omega_0}}\mathbf{J}(\mathbf{x},\omega), \quad (13)$$

$$\mathbf{K}'(\mathbf{x},\omega')\equiv\mathbf{K}(\mathbf{x},\omega). \quad (14)$$

The EM field equations in time-domain for the corresponding factitious dielectric model are, accordingly,

$$-\nabla\times\mathbf{H}'(\mathbf{x},t')+\varepsilon'(\mathbf{x})\frac{\partial\mathbf{E}'(\mathbf{x},t')}{\partial t'}=-\mathbf{J}'(\mathbf{x},t'), \quad (15)$$

$$\nabla\times\mathbf{E}'(\mathbf{x},t')+\mu\frac{\partial\mathbf{H}'(\mathbf{x},t')}{\partial t'}=-\mathbf{K}'(\mathbf{x},t'). \quad (16)$$

These results establish a theoretical one-to-one relationship between EM forward problem in a conductive medium and the EM forward problem in its corresponding dielectric model. Mittet (2010) shows how to solve CSEM forward problems in frequency-domain solving numerically the corresponding time-domain equations in the fictitious dielectric model. Initially he computes the current density in the fictitious domain, by least-squares fitting $\mathbf{J}'(\mathbf{x},t')$ to the field recorded $\mathbf{J}(\mathbf{x},\omega)$ using equation (13),

$$\mathbf{J}(\mathbf{x},\omega)=\sqrt{\frac{-2\omega_0}{i\omega}}\int_0^T dt'\mathbf{J}(\mathbf{x},t')e^{-\sqrt{\omega\omega_0}t'}e^{i\sqrt{\omega\omega_0}t'}. \quad (17)$$

Solving (15) e (16) by finite-differences in time-domain (FDTD) equations, the electric field in the conductive medium can be synthetized on the fly from equation (11):

$$\mathbf{E}(\mathbf{x},\omega)=\int_0^T dt'\mathbf{E}'(\mathbf{x},t')e^{-\sqrt{\omega\omega_0}t'}e^{i\sqrt{\omega\omega_0}t'}. \quad (18)$$

Adjoint-state method for inversion fictitious domain

Inversion of EM data for the estimation of subsurface resistivity is a nonlinear problem, which is usually solved using iterative optimization algorithms. For most of these algorithms, at each iteration, the resistivity model is updated based on the gradient of the misfit objective-function. The gradient of an objective-function can computed very efficiently through the adjoint-state method (Chavent, 2010).

The least-squares objective-function for the inversion of EM data in frequency-domain in a conductive medium, $\chi(\boldsymbol{\sigma})$, is

$$\chi(\boldsymbol{\sigma})=\sum_s\sum_r\sum_\omega\frac{W^E(\mathbf{x}^r,\mathbf{x}^s,\omega)}{2}\left\|\mathbf{E}^{obs}(\mathbf{x}^r,\omega;\mathbf{x}^s)-\mathbf{E}(\mathbf{x}^r,\omega;\mathbf{x}^s|\boldsymbol{\sigma}(\mathbf{x}))\right\|^2, \quad (19)$$

where the summation over all sources is indicated by index s, the summation over all receiver positions is indicated by superscript r and, the summation over all recorded frequencies is indicated by ω. W^E is a weighting factor which penalizes the misfit between the modeled and observed field components (Plessix and Mulder, 2008); $\mathbf{E}^{obs}(\mathbf{x}^r,\mathbf{x}^s,\omega)$ corresponds to the observed electric field at the receiver position $\mathbf{x}^r$, due to a source located at $\mathbf{x}^s$, for frequency ω; $\mathbf{E}(\mathbf{x}^r,\mathbf{x}^s,\omega)$ is the corresponding modeled field.

We apply the adjoint-state method to derive the gradient of $\chi(\boldsymbol{\sigma})$ relative to the model conductivity. This method can be understood as an extension of the Lagrange multipliers method. We start from a Lagrangian functional which contains the least-squares fitting objective function added to constraints which enforce that the modeled fields and medium properties should honor the Maxwell equation, i.e.,

$$\begin{aligned}\mathscr{L}(\mathbf{E},\mathbf{H},\boldsymbol{\sigma},\boldsymbol{\lambda}^E,\boldsymbol{\lambda}^H)=&\\ \sum_s\sum_\omega\sum_r\frac{W^E(\mathbf{x}^r,\omega;\mathbf{x}^s)}{2}&\left\|\mathbf{E}^{obs}(\mathbf{x}^r,\omega;\mathbf{x}^s)-\mathbf{E}(\mathbf{x}^r,\omega;\mathbf{x}^s|\boldsymbol{\sigma})\right\|^2\\ +\sum_s\sum_\omega&\Re\left(\int_\Omega d\Omega\boldsymbol{\lambda}^{E*}(\mathbf{u})\left[-\nabla\times\mathbf{H}(\mathbf{u})+\boldsymbol{\sigma}(\mathbf{x})\mathbf{E}+\mathbf{J}(\mathbf{u})\right]\right)\\ +\sum_s\sum_\omega&\Re\left(\int_\Omega d\Omega\boldsymbol{\lambda}^{H*}(\mathbf{u})\left[\nabla\times\mathbf{E}(\mathbf{u})-i\omega\mu\mathbf{H}(\mathbf{u})\right]\right) \quad (20)\end{aligned}$$

where $\mathbf{u}\equiv(\mathbf{x},\omega;\mathbf{x}^s)$ and $\Re(z)$ indicates the real part of its complex argument, z, and the adjoint-state fields, $\boldsymbol{\lambda}^E(\mathbf{x},\omega;\mathbf{x}^s)$ and $\boldsymbol{\lambda}^H(\mathbf{x},\omega;\mathbf{x}^s)$, are determined imposing the condition that the Lagrangian should be stationary relative to first order variations on the EM fields (Plessix, 2006; Chavent, 2010).

Requiring the first variation of the Lagrangian functional relative to the modeled EM fields and model conductivity to be stationary relative to EM fields perturbations, one obtains the system of equations for the adjoint-state fields $\boldsymbol{\lambda}^E$ and $\boldsymbol{\lambda}^H$,

$$\begin{aligned}\nabla\times\boldsymbol{\lambda}^{H*}(\mathbf{u})+\boldsymbol{\sigma}(\mathbf{x})\boldsymbol{\lambda}^{E*}(\mathbf{u})=&\\ \sum_r\delta(\mathbf{x}-\mathbf{x}^r)W^E(\mathbf{u})&\left[\mathbf{E}^{obs}(\mathbf{u})-\mathbf{E}(\mathbf{u})\right], \quad (21)\end{aligned}$$

$$-\nabla\times\boldsymbol{\lambda}^{E*}(\mathbf{u})-i\omega\mu\boldsymbol{\lambda}^{H*}(\mathbf{u})=\mathbf{0}, \quad (22)$$

and the gradient of the objective function relative to the conductivity tensor

$$\left.\frac{\partial\chi}{\partial\boldsymbol{\sigma}}\right|_{\mathbf{x}}=\sum_s\sum_\omega\Re\left\{\boldsymbol{\lambda}^{E*}(\mathbf{x},\omega;\mathbf{x}^s)\mathbf{E}(\mathbf{x},\omega;\mathbf{x}^s)\right\}. \quad (23)$$

Therefore, after solving the adjoint-state equations, one can evaluate the gradient of the objective function relative to the conductivity.

Based on Mittet (2010) we derived the solution of equations (21) and (22) using the correspondence principle. Our derivation shows that the corresponding adjoint-field equations in the fictitious dielectric medium in frequency-domain are:

$$-\nabla\times\boldsymbol{\lambda}^{H'}(\mathbf{x},\omega')+(-i\omega')\varepsilon'(\mathbf{x})\boldsymbol{\lambda}^{E'}(\mathbf{x},\omega') = -\sum_r \delta(\mathbf{x}-\mathbf{x}^r)\mathbf{J}'(\mathbf{x},\omega'), \quad (24)$$

$$\nabla\times\boldsymbol{\lambda}^{E'}(\mathbf{x},\omega')+(-i\omega')\mu\boldsymbol{\lambda}^{H'}(\mathbf{x},\omega')=\mathbf{0}. \quad (25)$$

The relations between the adjoint-state equations in conductive and the corresponding adjoint-state equation in the fictitious dielectric medium derive from the identifications:

$$\omega' \equiv (1-i)\sqrt{\omega\omega_0}, \quad (26)$$

$$\varepsilon'(\mathbf{x}) \equiv \boldsymbol{\sigma}(\mathbf{x})/(2\omega_0), \quad (27)$$

$$\boldsymbol{\lambda}^{E'}(\mathbf{x},\omega') \equiv \boldsymbol{\lambda}^{E*}(\mathbf{x},\omega), \quad (28)$$

$$\boldsymbol{\lambda}^{H'}(\mathbf{x},\omega') \equiv -\sqrt{\frac{-i\omega}{2\omega_0}}\boldsymbol{\lambda}^{H*}(\mathbf{x},\omega), \quad (29)$$

$$\mathbf{J}'(\mathbf{x},\omega') \equiv -\sqrt{\frac{-i\omega}{2\omega_0}}\Delta\mathbf{E}^*(\mathbf{x},\omega). \quad (30)$$

These correspondence relations should be compared with equations (9)-(14) for the EM fields. Equations (26)-(30) allow the transformation of time-domain adjoint-state fields to the corresponding frequency-domain adjoint-state fields in the conductive medium. We start transforming the system of equations (24) and (25) to time-domain:

$$-\nabla\times\boldsymbol{\lambda}^{H'}(\mathbf{x},t')+\varepsilon'(\mathbf{x})\partial_t'\boldsymbol{\lambda}^{E'}(\mathbf{x},t') = -\sum_r \delta(\mathbf{x}-\mathbf{x}^r)\mathbf{J}'(\mathbf{x},t'), \quad (31)$$

$$\nabla\times\boldsymbol{\lambda}^{E'}(\mathbf{x},t')+\mu\partial_t'\boldsymbol{\lambda}^{H'}(\mathbf{x},t')=\mathbf{0}, \quad (32)$$

subjected to homogeneous final conditions, i.e., $\boldsymbol{\lambda}^{E'}(\mathbf{x},T)=\mathbf{0}$ and $\boldsymbol{\lambda}^{H'}(\mathbf{x},T)=\mathbf{0}$ all over the modeled domain and homogeneous boundary conditions on the domain boundary. We can now use the algorithm introduced by Mittet (2010) to solve these equations numerically through finite-difference. The current density to be injected at each receiver position is constrained by the correspondence relation in equation (30):

$$\Delta\mathbf{E}^*(\mathbf{x}^r,\omega)=\sqrt{\frac{-2\omega_0}{i\omega}}\int_0^T dt'\mathbf{J}(\mathbf{x}^r,t')e^{-\sqrt{\omega\omega_0}t'}e^{i\sqrt{\omega\omega_0}t'}, \quad (33)$$

Finally, the adjoint field $\boldsymbol{\lambda}^{E*}(\mathbf{x},\omega)$ is evaluated on the fly at each finite-difference time-update using the correspondence relation in equation (28):

$$\boldsymbol{\lambda}^{E*}(\mathbf{x},\omega)=-\int_0^T \boldsymbol{\lambda}^{E'}(\mathbf{x},t')e^{-\sqrt{\omega\omega_0}t'}e^{i\sqrt{\omega\omega_0}t'}dt'. \quad (34)$$

Sources for the adjoint-state equations

The estimation of the current density distribution $\mathbf{J}'(\mathbf{x},t')$ for (31) is an important aspect in our implementation. At each optimization iteration, for the receiver at $\mathbf{x}^r$, the components $J_i'(\mathbf{x}^r,t')$ are estimated from the corresponding electric field residual components in frequency-domain, $\Delta E_i(\mathbf{x}^r,\omega_m)=E_i^{obs}(\mathbf{x}^r,\omega_m)-E_i(\mathbf{x}^r,\omega_m)$, for the set of recorded frequencies, ω_m, with $m\in\{1,\cdots,N_\omega\}$.

The discretization of equation (33) produces the linear system:

$$\Delta E_i^*(\mathbf{x}^r,\omega_m)=\sum_{n=1}^{N_t}A_{mn}J_i'(\mathbf{x}^r,t_n'), \quad (35)$$

where

$$A_{mn}=\Delta t'\sqrt{\frac{-2\omega_0}{i\omega_m}}e^{-\sqrt{\omega_m\omega_0}t_n'}e^{i\sqrt{\omega_m\omega_0}t_n'}. \quad (36)$$

This linear system is highly ill-conditioned. To assure stability and uniqueness to the solution of (35) we use model reparameterization (Harlan, 1995; Claerbout, 2003),

$$\mathbf{J}_i'=\mathbf{PWm}. \quad (37)$$

and an additional set of ridge regression equations (Menke, 2018), with damping parameter λ_t,

$$\begin{pmatrix}\mathbf{AP}\\ \lambda_t\mathbf{I}\end{pmatrix}\mathbf{Wm}=\begin{pmatrix}\Delta\mathbf{E}_i^*\\ \mathbf{0}\end{pmatrix}. \quad (38)$$

We solve this linear system using least-squares conjugate gradient (Claerbout, 2003).

In equation (37), our choice for the operator $\mathbf{P}$, was a smoothing preconditioning operator, in which each row corresponds to a Ricker pulse,

$$P_{nk}=\left(1-2\pi f_p(t_n-t_k)^2\right)e^{-\pi f_p(t_n-t_k)^2}, \quad (39)$$

enforces a zero-mean pulse in time-domain and warrants a casual response; the diagonal weight matrix $\mathbf{W}$

$$W_{nn}=e^{-\pi f_p t_n}, \quad (40)$$

promotes a minimum-delay pulse (Claerbout, 2003).

Model regularization and constraints

Traditionally, to stabilize the non-linear inversion a commonly regularization is maximun smoothness, which is take as finite difference approximation of Laplacian operator (Cai et al., 2021). We used the model reparameterization proposed by Harlan (1995). In this case, we assume

$$\boldsymbol{\sigma}=\mathbf{S}^3\mathbf{S}^2\mathbf{S}^1\mathbf{p}, \quad (41)$$

where $\mathbf{S}^i$ indicates the smoothing operator acting along the i-coordinate direction and $\mathbf{p}$ the auxiliary parameter vector updated at each optimization iteration. So instead of insert a regularization parameter, the smooth model is modeled directly, without disregard the heterogeneities. Consequently, the gradient used by the iterative optimizer is

$$\frac{\partial\chi}{\partial p_{ijk}}=\frac{\partial\chi}{\partial\sigma_{lmn}}\frac{\partial\sigma_{lmn}}{\partial p_{ijk}}=S_{kn}^3S_{jm}^2S_{il}^1\frac{\partial\chi}{\partial\sigma_{lmn}}, \quad (42)$$

where summation convention is assumed on repeated indexes. We use an exponential filter (Hale, 2012) along the i-coordinate direction to implement $\mathbf{S}^i$.

To further taylor the inversion results, we limit the model electric conductivity to the interval (σ_L,σ_U), thus enforcing a priori information usually available about the geological scenario for the inversion. Accordingly, we follow Bording et al. (2021) and use the change of variables:

$$\boldsymbol{\sigma}=\left(\frac{\sigma_U+\sigma_L}{2}\right)+\left(\frac{\sigma_U-\sigma_L}{2}\right)\left(\frac{e^\gamma-1}{e^\gamma+1}\right). \quad (43)$$

where $\gamma\in\mathbb{R}$ and is unbounded.

Numerical experiments

We validate our implementation in a simple isotropic reservoir model proposed by Støren et al. (2008). Figure 1 (a) shows a vertical section of the resistivity model, which is translation invariant along the direction normal to this section and has a reservoir with $25\ \Omega m$ and dimensions $4.2\ km$ in x-coordinate and $0.4\ km$ in z-coordinate. The initial model for all the inversion experiments, which also

is translation invariant, is in Figure 1 (b).

The model has $18\ km$ in the east-west direction (x-coordinate), $10\ km$ in north-south direction (y-coordinate) and, $3\ km$ of depth (z-coordinate). For the numerical computations the model sampled in a mesh of $0.1\ km$ along z and, $0.2\ km$ along x and y directions. The acquisition geometry has receivers at every $0.1\ km$ in x arranged in the center of the model with respect to the y extension. All receivers are at $0.65\ km$ of depth. The sources are located from $6\ km$ to $12\ km$ with $1\ km$ interval. The fields are sampled at a time rate of $20\ ms$. We computed the synthetic data set with our implementation of the Mittet algorithm (Mittet, 2010).

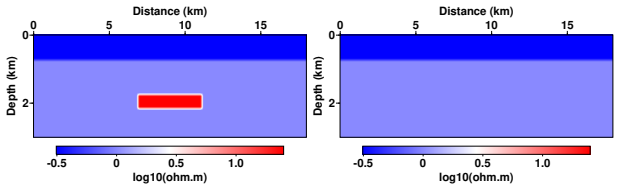

Figura 1: Resistivity models used to obtain a) the observed and b) the calculated synthetic data

Figure 2 presents the amplitude and phase of the fields for the frequencies that we use in all the inversion experiments: 0.25 Hz, 0.50 Hz and 0.75 Hz. One can see the extension where the air-waves dominate the signal and how it decreases with the frequency increase.

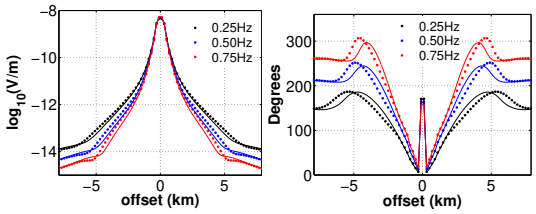

Figura 2: a) Amplitude and b) phase of the electric field, for the observed data (solid line) and calculated data (dotted line).

One important point to assure the accuracy of the inversion based on the correspondence principle is how the source pulse in time-domain, in the fictitious dielectric medium, fits the electric field observations, in frequency-domain. Figure 3 illustrates that our strategy for the source pulse estimation fits accurately the observed data.

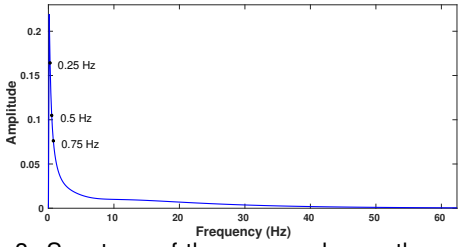

Figura 3: Spectrum of the ource pulse on the conductive medium (solid curve), computed with equation (33). The black dots indicate observed data in frequency-domain.

We apply to post-processing steps to gradient of object-function to avoid artifacts in the inversion results. We muted the gradient around the receivers depth to remove spurious high-amplitude values and we preconditioned the gradient using amplitude compensation, i.e., dividing the gradient by the energy of the source field. Figure 4 shows the post-processed gradient for the frequencies 0.25 Hz and 0.75 Hz. Due to this procedure one can somehow identify an anomaly in the middle portion of the gradient associated with the reservoir.

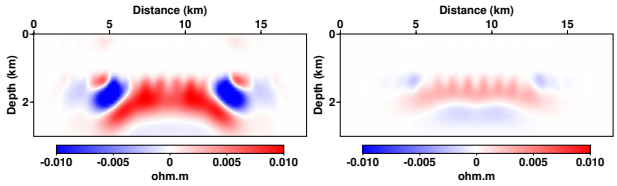

Figura 4: Muted gradient, with amplitude compensation for the frequencies a) $0.25\ Hz$ and b) $0.75\ Hz$.

The regularization using model reparameterization differ for the two inversion algorithms. For the ADAM algorithm, we use an exponential window with half-length equal to a single mesh interval for smoothing along depth, and an exponential window with half-length of two mesh intervals for smoothing the model horizontally. For the LBFGS algorithm, the exponential smoothing window has half-length of single mesh interval along all coordinate directions.

We performed two inversion experiments for each inversion algorithm. The first, using a single frequency data set of 0.25 Hz. The second, using multiple frequencies data set with 0.25 Hz, 0.50 Hz and 0.75 Hz. We also assumed model translation invariance along the y-direction in all the inversions.

The Figure 5 (a) shows the resistivity model obtained after 38 iterations for the single frequency data set. Figure 5 (b) shows the resistivity model after 51 ADAM iterations using the multiple frequency data set. The single frequency result better recovered the location and thickness of the reservoir, however the resistivity contrast were underestimated. Figure 6 shows the corresponding inversion results for LBFGS algorithm. Figure 6 (a) shows the resistivity model after 7 iterations for the single frequency data set and, Figure 6 (b) presents the resistivity model after 5 iterations for the multi-frequency data set. Again, the single frequency result estimated a better location for the reservoir. The two inversions recover well the resistivity contrast and over-estimated the reservoir thickness. Observe that a single iterations of the LBFGS algorithm might need several evaluations of the objective-function and its gradient at the line-search phase of this algorithm. The ADAM algorithm has no line-search.

Finally, Figures 5 and 6 show that all the models estimated are consistent with the data used run the inversion. The models estimated with the ADAM algorithm produce a slight better data fit when compared with the corresponding models estimated using the LBFGS.

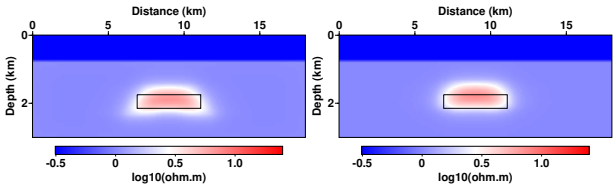

Figura 5: Resistivity model estimated using the ADAM algorithm. a) for the single frequency data set, 0.25 Hz and b) for the multi-frequency data set. The black rectangle indicates the exact reservoir location.

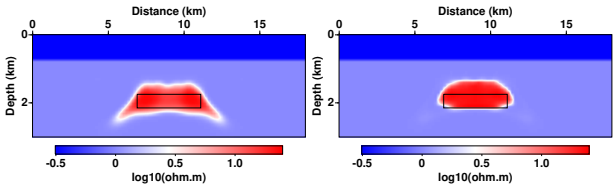

Figura 6: Resistivity model estimated using the LBFGS algorithm. a) for the single frequency data set, 0.25 Hz and b) for the multi-frequency data set. The black rectangle indicates the exact reservoir location.

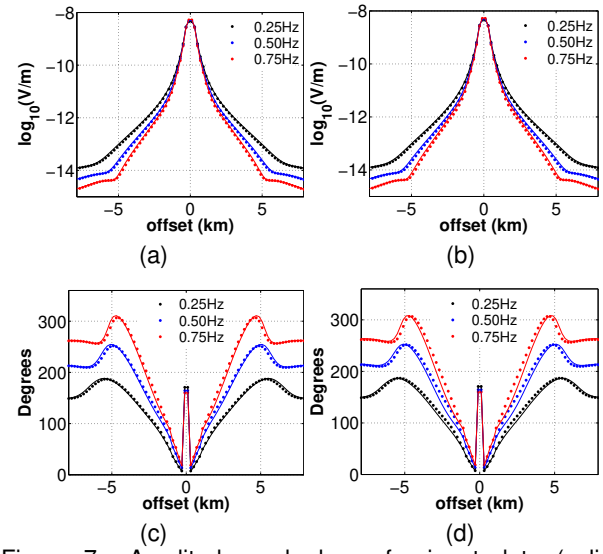

Figura 7: Amplitude and phase for input data (solid lines) and corresponding fit produced by the estimated models using ADAM algorithm (dotted lines): (a) single-frequency inversion amplitudes, (b) multi-frequency inversion amplitudes; (c) single-frequency inversion phases, (d) multi-frequency inversion phase.

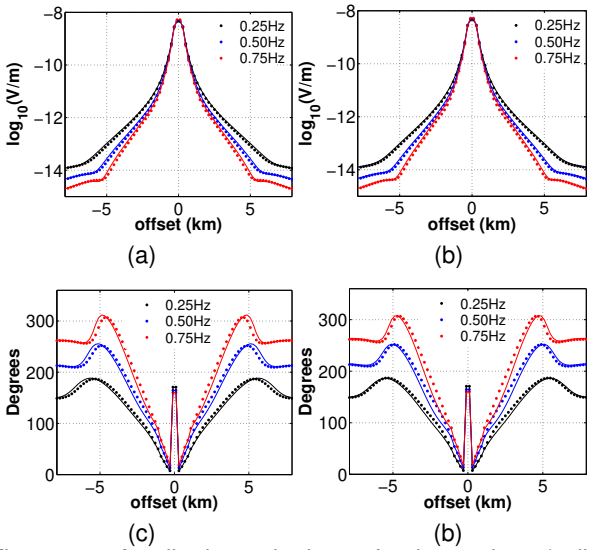

Figura 8: Amplitude and phase for input data (solid lines) and corresponding fit produced by the estimated models using LBFGS algorithm (dotted lines): (a) single-frequency inversion amplitudes, (b) multi-frequency inversion amplitudes; (c) single-frequency inversion phases, (d) multi-frequency inversion phase.

Discussion

We use the adjoint-state method to derive the correspondence between the inversion of CSEM and the inversion of the electric permittivity in a dielectric medium based on the correspondence principle (de Hoop, 1996; Mittet, 2010). This derivation shows how to compute the contribution of each source to the gradient of CSEM inversion using two finite-differences simulations in the dielectric corresponding medium in time-domain. A forward in time simulation do compute the fitting data and a reverse-time simulation to back-propagate the residuals between the observed and modeled data set. Our numerical implementation of the inversion based on this formulation was successfully validated for a synthetic data set computed from a resistivity model representing a simple reservoir. Another feature of our inversion algorithm also validated by our numerical experiments is the use of smoothing operators to stabilize the non-linear inversion using model reparameterization. Our numerical experiments show that this approach is effective in tailoring the inverted model according to the design of the smoothing operators (Ma et al., 2012). An attractive feature of using the FDTD solution of Maxwell's equations as the modeling driver for CSEM inversion is that it can be remarkably accelerated when implemented on GPUs, thus improving the efficiency CSEM inversion of large 3D resistivity models.

Conclusion

The inversion of CSEM data in the frequency domain can be mapped into an equivalent inversion of time-domain EM fields in a dielectric fictitious medium using the correspondence principle. To reach this result, our derivation adds to the already known mapping between the EM forward problem in a conductive medium and the forward problem in a fictitious dielectric medium another mapping, between the adjoint-state equations

in a conductive and the adjoint-state equations in the corresponding dielectric medium. Once the forward modeling and adjoint-state field are available, the gradient of the least-squares objective function relative to the medium resistivity is determined. The inversion can then proceed using an iterative optimization algorithm. The validation of this procedure for CSEM inversion on a synthetic data set computed for a 3D simple reservoir model estimated models consistent with the data. The spatial resolution of the estimated modes depends on the optimizer and the choice of regularization. Regularization using model reparameterization proved very useful for this application when compared to Tikhonov regularization. No regularizing functional needs to be added to the data-fitting objective function. Therefore, no trial and error procedure to choose a regularization parameter needs to be performed to enforce the desired penalization on the solution.

Acknowledgements

The authors would like to thank to CAPES and CNPq for the scholarships, PETROBRAS, CPGf/UFPA and INCT-GP in Petroleum Geophysics for the support to the research.

Referências

Bording, T. S., M. R. Asif, A. S. Barfod, J. J. Larsen, B. Zhang, D. J. Grombacher, A. V. Christiansen, K. W. Engebretsen, J. B. Pedersen, P. K. Maurya, et al., 2021, Machine learning based fast forward modelling of ground-based time-domain electromagnetic data: Journal of Applied Geophysics, **187**, 104290.

Cai, H., Z. Long, W. Lin, J. Li, P. Lin, and X. Hu, 2021, 3d multinary inversion of controlled-source electromagnetic data based on the finite-element method with unstructured mesh: Geophysics, **86**, E77–E92.

Chavent, G., 2010, Nonlinear least squares for inverse problems – theoretical foundations and step-by-step guide for applications: Springer Netherlands. Scientific Computation, No. 1.

Claerbout, Jon F. e Fomel, S., 2003, Image estimation by example: Geophysical soundings image construction - multidimensional autoregression.

de Hoop, A. T., 1996, A general correspondence principle for time-domain electromagnetic wave and diffusion fields: Geophysical Journal International, **127**, 757–761.

Hale, D., 2012, My favorite ten-line computer program: https://inside.mines.edu/~dhale/notebook.html. (Accessed: 2021-05-30).

Hansen, K., M. Panzner, D. Shantsev, and R. Mittet, 2016, Tti inversion of marine csem data, *in* SEG Technical Program Expanded Abstracts 2016: Society of Exploration Geophysicists, 1014–1018.

Harlan, W. S., 1995, Regularization by model reparameterization: Citeseer.

Hoversten, G. M., R. L. Mackie, and Y. Hua, 2021, Reexamination of controlled-source electromagnetic inversion at the lona prospect, orphan basin, canada: Geophysics, **86**, E157–E170.

Kingma, D. P., and J. Ba, 2014, Adam: A method for stochastic optimization: arXiv preprint arXiv:1412.6980.

Lima, W. A., J. B. Silva, D. F. Santos, and J. C. Costa, 2019, A robust interactive estimation of the regularization parameter: Geophysics, **84**, IM19–IM33.

Ma, Y., D. Hale, B. Gong, and Z. Meng, 2012, Image-guided sparse-model full waveform inversion: Geophysics, 77: R189–R198.

Meju, M. A., R. L. Mackie, F. Miorelli, A. S. Saleh, and R. V. Miller, 2019, Structurally tailored 3d anisotropic controlled-source electromagnetic resistivity inversion with cross-gradient criterion and simultaneous model calibration: Geophysics, **84**, E387–E402.

Meju, M. A., A. S. Saleh, R. L. Mackie, F. Miorelli, R. V. Miller, and N. K. S. Mansor, 2018, Workflow for improvement of 3d anisotropic csem resistivity inversion and integration with seismic using cross-gradient constraint to reduce exploration risk in a complex fold-thrust belt in offshore northwest borneo: Interpretation, **6**, SG49–SG57.

Menke, W., 2018, Geophysical data analysis: Discrete inverse theory: Academic press.

Mittet, R., 2010, High-order finite-difference simulations of marine csem surveys using a correspondence principle for wave and diffusion fields fdtd simulation of marine csem surveys: Geophysics, **75**, F33–F50.

Nguyen, A. K., J. I. Nordskag, T. Wiik, A. K. Bjørke, L. Boman, O. M. Pedersen, J. Ribaudo, and R. Mittet, 2016, Comparing large-scale 3d gauss–newton and bfgs csem inversions, *in* SEG Technical Program Expanded Abstracts 2016: Society of Exploration Geophysicists, 872–877.

Plessix, R.-E., 2006, A review of the adjoint-state method for computing the gradient of a functional with geophysical applications: Geophysical Journal International, **167**, 495–503.

Plessix, R.-E., and W. Mulder, 2008, Resistivity imaging with controlled-source electromagnetic data: Depth and data weighting: Inverse problems, **24**, 034012.

Støren, T., J. Zach, and F. Maaø, 2008, Gradient calculations for 3d inversion of csem data using a fast finite-difference time-domain modelling code: Presented at the 70th EAGE Conference and Exhibition incorporating SPE EUROPEC 2008.

Zhu, C., R. H. Byrd, P. Lu, and J. Nocedal, 1997, Algorithm 778: L-bfgs-b: Fortran subroutines for large-scale bound-constrained optimization: ACM Transactions on Mathematical Software (TOMS), **23**, 550–560.